Supporting Information

Sponge Effect Boosting Oxygen Reduction Reaction at the Interfaces between Mullite $SmMn_2O_5$ and Nitrogen-Doped Reduced Graphene Oxide

Meng Yu, Li Wang, Jieyu Liu, Hui Li, Xiuyao Lang, Chunning Zhao, Zhanglian Hong and Weichao Wang*

1. Supplementary Texts

1.1 Sample preparations

Graphene Oxide. Graphene oxide (GO, 1% in water) was purchased from The Sixth Element (Changzhou) Materials Technology Co, Ltd, China.

Synthesis of SMO/ SMO@rGO-x/ SMO@NrGO-x. All metal salt precursors were analytical grade and used as received. In a typical synthesis of SMO@rGO-2, 117 mg $Sm(NO_3)_3 \cdot 6H_2O$ (Aladdin, China) and 3 ml GO were dissolved in deionized water (47 ml, 18.25 MΩ) assisted by 30 min ultrasonication, followed by adequate stirring. Then 16.7 mg $KMnO_4$ and 60.5 mg $Mn(CH_3COO)_2 \cdot 4H_2O$ (Aladdin, China) were added to the solution simultaneously and constantly stirred for at least 30 min. After that, 5.5 ml 1 M NaOH (96%, Aladdin, China) was slowly added to the above mentioned mixture and continued to stir for another 5 min. The obtained homogenous mixture was then transferred to a 100 ml stainless steel Teflon-lined autoclave and treated at 180 °C for 24 h. After that, the final product was filtrated and washed with diluted nitric acid (2%) and deionized water repeatedly for three times. To prepare SMO@rGO with different feeding ratios of SMO and GO (SMO@rGO-x), stoichiometric metal salt precursors were added following the similar procedure with the concentration of GO and NaOH keeping constant. Finally, the obtained precipitate was dried by lyophilization. Pure SMO was prepared without adding GO in the first step. To prepare SMO@NrGO-2, 1 ml ammonium hydroxide (25~28 %, Tianjin Jiangtian Chemicals, China) was added dropwise after NaOH.

Synthesis of NiFe LDH loaded Ni foam. The in-situ growth of NiFe LDH on Ni foam was achieved according to previous literature.[1] Briefly, 2.8 mmol $Ni(NO_3)_2 \cdot 6H_2O$, 0.4 mmol $Fe(NO_3)_3 \cdot 9H_2O$, 15 mmol urea and 6 mmol NH_4F were dissolved in 60 ml deionized water under vigorous stirring for 30 min and then transferred to a Teflon-lined autoclave. After that, a clean Ni foam was immersed vertically into the container. The autoclave was maintained at 120 ºC for 6 h. After naturally cooling down to room temperature, the final products were repeatedly washed with deionized water and ethanol and dried in vacuum at 60 °C overnight. The final mass loading of NiFe LDH was measured to be approximate 1.8 mg cm^{-2}.

1.2 Material Characterization

X-ray Diffraction (XRD) patterns were recorded using a Rigaku MiniFlex600 X-ray diffractometer with Cu Kα radiation (λ = 0.1542 Å) operating at 40 kV and 40 mA at a scan speed of 8 ° min^{-1} with an interval of 0.02°. The micro/nanostructures of the products were examined with JEOL JEM-2010FEF Field Emission Transmission Electron Microscopy (FETEM). X-ray Photoelectron Spectroscopy (XPS) measurements were performed with a Thermo Scientific ESCALAB 250Xi multifunctional X-ray photoelectron spectroscope. Nitrogen adsorption-desorption isotherms were measured at 77 K by a BeiShiDe Instrument 3H-2000PM2 specific surface and pore size analyzer. Infrared spectra were taken with the Thermo Scientifi Nicole iS10 FTIR spectrometer from 400 to 4000 cm^{-1}. Raman spectra were recorded using a SR-500I-A microconfocal Raman spectrometer (Oxford Instruments) with a 532 nm wavelength laser.

1.3 Powder resistance measurement

The resistance of powder sample was roughly measured with a home-made configuration as illustrated in Figure S16a. Specificaly, sample (~0.5 g) was placed into a conductive holder embedded in a hole in the center of a ceramic insulator. The diameter of the circular holder and the cynlindar hole were ~0.8 cm, leading to a cross section of ~0.5 cm^2. A conductive rod with the same cross section area and ~2 cm

in length was then placed on the top of sample to form a conductor-sample-conductor sandwitch structure. The whole setup was then transferred to a sheeting presser. By measuring the resistance between two conductors and the thickness of sample under different pressure, the specific resistance could be estimated.

1.4 Electrochemical Measurements

Most electrochemical measurements were carried out using an Autolab PGSTAT128N electrochemical working station in a three-electrode configuration at room temperature, using a catalyst-loaded rotating ring-disk electrode (RRDE) as working electrode, Hg/HgO as reference electrode and Pt foil as counter electrode. The electrolyte is 0.1 M KOH aqueous solution. In order to prepare the working electrode, catalyst inks were made by ultrasonically mixing 5 mg catalysts powder, 1 mg Vulcan XC-72 conductive carbon (Carbot Conp., USA), 100 μl deionized water, 850 ul absolute ethyl alcohol and 50 ul Nafion (5%, Alfa, USA). These inks were carefully dropped onto glassy carbon electrodes and dried under atmospheric environment at room temperature to achieve a catalyst loading of 250 μg cm^{-2}_{disk}. For ORR measurement, all the electrodes were first scanned in argon-saturated 0.1 M KOH for 30 cycles between 0.1 V and 1.2 V at 50 mV s^{-1} to obtain clean and stable surfaces. Linear sweep voltammetry (LSV) curves at 5 mV s^{-1} from 1.2 V to 0.1 V were recorded as background currents. The ORR polarization curves were obtained by recording LSV in oxygen-saturated 0.1 M KOH followed after background subtraction. All the potential in this work was referred to reverse hydrogen electrode (RHE) scale by $E_{RHE} = E_{detected} + 0.098\ V + 0.059pH$ after iR-compensation. The solution resistance between working and reference electrode was measured by electrochemical impendence spectroscopy (EIS) with an alternating current (AC) voltage of 5 mV in amplitude between 10 kHz and 0.1 Hz at 0.85 V. For OER measurements, nickel foam supported NiFe layered double hydroxide or RuO_2 (~1.8 mg cm^{-2}) was directly used as working electrode with 1 M KOH as electrolyte, and polarization curves were collected by LSV at 5 mV s^{-1} between 1.2 V and 1.8 V.

The Tafel slope was obtained from Tafel's equation:

$$\eta = a + blgJ_K \quad \text{(S1)}$$

where η represented the overpotential, and J_K was the kinetic current density with mass-transport correction by

$$J_K = \frac{J_L \times J}{J_L - J} \quad \text{(S2)}$$

The number of elelctron transferred and yield of peroxide were calculated by

$$n = \frac{4I_D}{I_D + {}^{I_R}/_{N_c}} \quad \text{(S3)}$$

$$\%HO_2^- = 100 \times \frac{2({}^{I_R}/_{N_c})}{I_D + {}^{I_R}/_{N_c}} \quad \text{(S4)}$$

where I_D and I_R are the disk and ring current, respectively. N_C is the calibrated collection efficiency.

1.5 Full Battery Assembly and Tests

Aqueous Zn-Air Battery Assembly. The Zn-air batery was made using Zn plate as anode, catalyst-loaded composite gas diffusion electrode (GDE) as cathode and aqueous 6 M KOH and 0.2 M $Zn(CH_3COO)_2$ solution as electrolyte. Catalyst inks were prepared by added 5 mg catalyst (SMO@NrGO-2 or Pt/C) and 5 mg Vulcan XC-72 conductive carbon into a mixture containing 1 ml ethanol, 0.25 ml deionized water and 50 μl Nafion, followed by 30 min ultrasonication. 5 mg RuO_2 was also added to the Pt/C ink for rechargeable ZAB. To prepare the GDE, catalyst was first loaded onto a carbon paper (1.13 cm^2) via drop-casting to achieve a final loading of 1.5 $mg_{catalyst}$ cm^{-2}. Then the as-prepared carbon paper, Ni foam (NiFe LDH loaded Ni foam for ZAB made with SMO@NrGO-2) and waterproof breathable member were placed layer-by-layer orderly and pressed under 2 MPa for 1 min with a sheeting presser.

1.6 Density functional theory (DFT) calculations

In this work, all density functional theory (DFT) calculations were performed through the Vienna Ab Initio Simulation Package (VASP) code. [2, 3] To estimate the exchange and correlation energy, generalized gradient approximations (GGA) with Perdew-Burke-Ernzerhof (PBE) was chosen.[4] The

interactions between electron and ion were described by using projector augmented wave (PAW) method.[5] For composite system, the van der Walls interaction (vdWs) was considered with the DFT+D_3 method applied, which is empirical correction in Grimme's scheme.[6] The cutoff energies of 400 eV were employed on the basis of plane waves. As shown in Figure S12b-d, three different structures were built to simulate N doping configurations, i.e., graphitic, pyrrolic, and pyridinic N, respectively.[7] Spin polarization was carried out in all calculations. During the relaxing of structures, the converged energy criterion was 10^{-4} eV and the optimization was performed until the force on each atom was smaller than 0.05 eV $Å^{-1}$. The upper half of slabs and adsorbates were relaxed with others were fixed. Besides, with a smearing width of 0.05 eV, the Gaussian smearing was used. As for the interactions between periodic image slabs, a vacuum with thickness of 15 Å was adopted to avoid them.

The four-electron pathway was considered in this work:

$$O_2 + e^- + OH^* \longrightarrow OO^* + OH^- \quad \text{(S5)}$$

$$OO^* + e^- + H2O \rightarrow OOH^* + OH^- \quad \text{(S6)}$$

$$OOH^* + e^- \rightarrow O^* + OH^- \quad \text{(S7)}$$

$$O^* + e^- + H2O \rightarrow OH^* + OH^- \quad \text{(S8)}$$

At zero cell potential (U=0), the Gibbs free energy (ΔG) for every elementary reaction step can be calculated as follows:

$$\Delta G_1 = G_{OO*} + G_{OH-} - G_{e-} - G_{OH*} - G_{O2} \quad \text{(S9)}$$

$$= G_{OO*} + (G_{H2O} - {}^{1}/_{2}G_{H2}) - G_{OH*} - (2G_{H2O} - 2G_{H2} + 4.92)$$

$$= \Delta G_{OO^*} - \Delta G_{OH^*} - 4.92$$

$$\Delta G_2 = G_{OOH*} + G_{OH-} - G_{e-} - G_{OO*} - G_{H2O} \quad \text{(S10)}$$

$$= G_{OOH*} - G_{OO*} - {}^{1}/_{2}G_{H2}$$

$$= \Delta G_{OOH^*} - \Delta G_{OO^*}$$

$$\Delta G_3 = G_{O*} + G_{OH-} - G_{e-} - G_{OOH*} \quad \text{(S11)}$$

$$= G_{O*} - G_{OOH*} + G_{H2O} - {}^{1}/_{2} G_{H2}$$

$$= \Delta G_{O^*} - \Delta G_{OOH^*}$$

$$\Delta G_4 = G_{OH*} + G_{OH-} - G_{e-} - G_{O*} - G_{H2O} \quad \text{(S12)}$$

$$= G_{OH*} - G_{O*} - {}^{1}/_{2} G_{H2}$$

$$= \Delta G_{OH^*} - \Delta G_{O^*}$$

2. Supplementary Figures and Tables

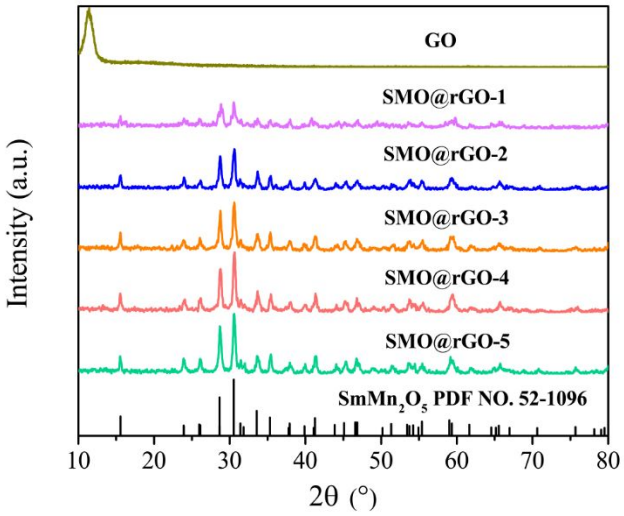

Figure S1. XRD spectra of GO and SMO@rGO-x.

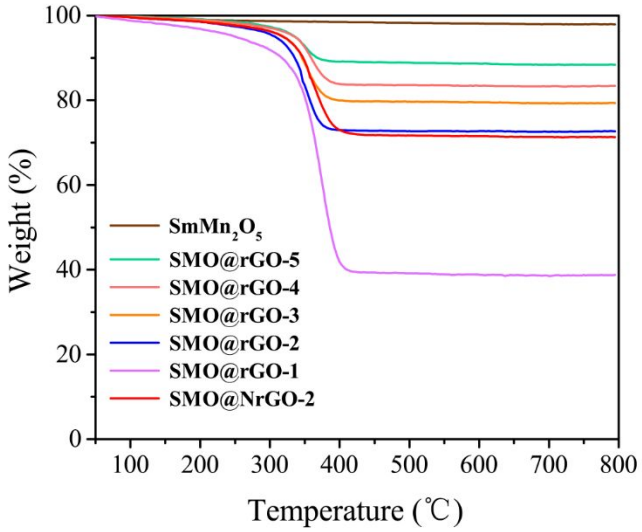

Figure S2. Thermogravimetric plots of $SmMn_2O_5$, SMO@rGO-x and SMO@NrGO-2 under air flow.

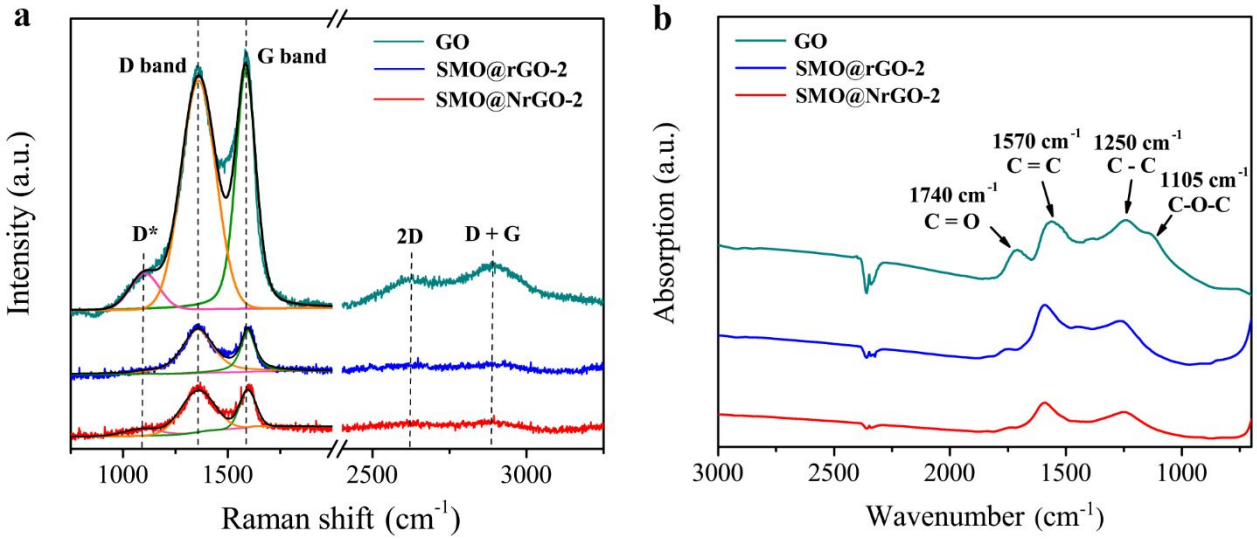

Figure S3. (a) Raman spectra and (b) FTIR spectra of GO, SMO@rGO-2 and SMO@NrGO-2.

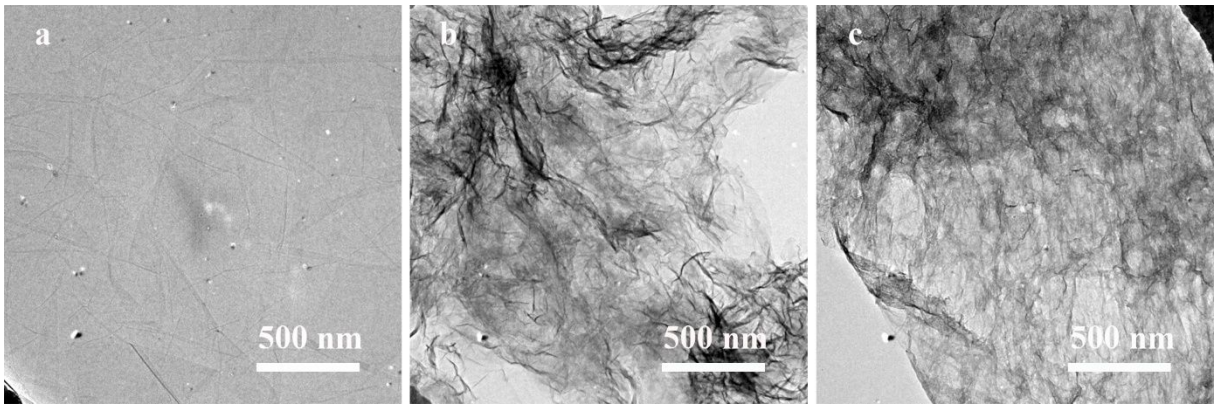

Figure S4. TEM images of (a) GO, (b) rGO and (c) NrGO.

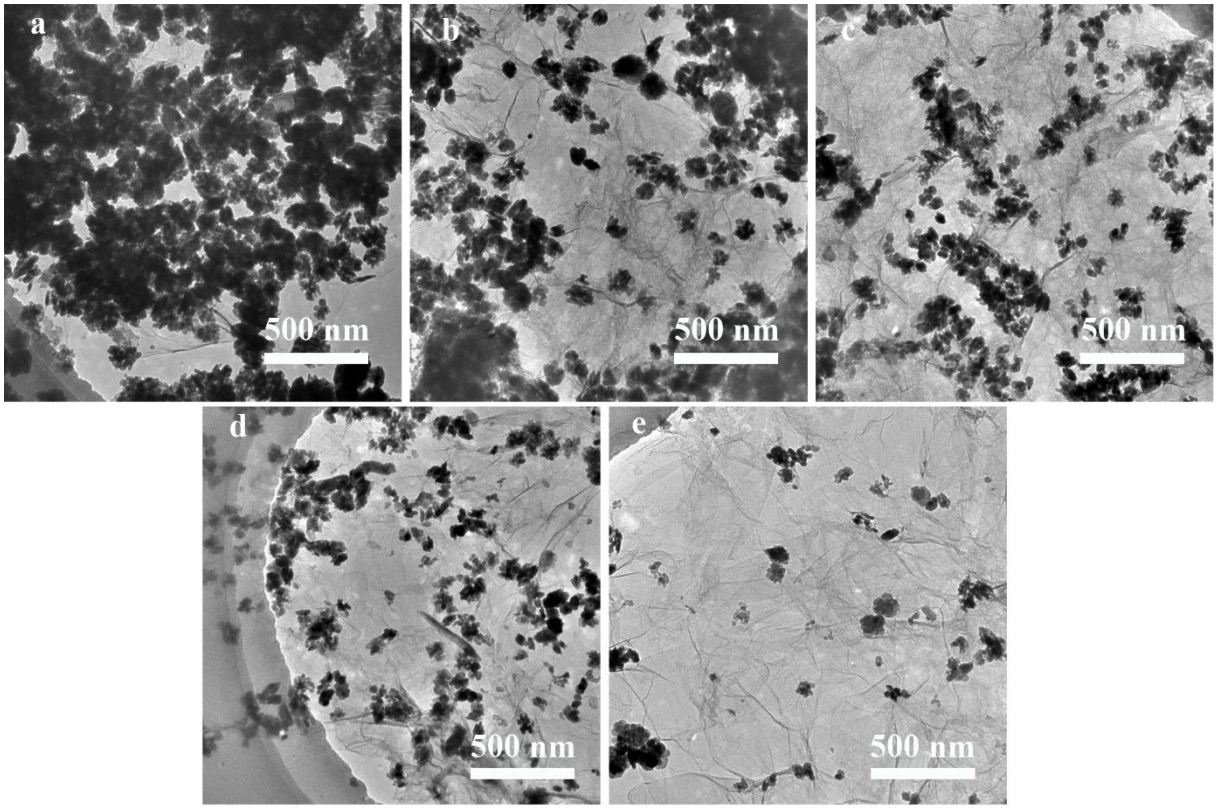

Figure S5. TEM images of (a) SMO@rGO-5, (b) SMO@rGO-4, (c) SMO@rGO-3, (d) SMO@rGO-2 and (e) SMO@rGO-1.

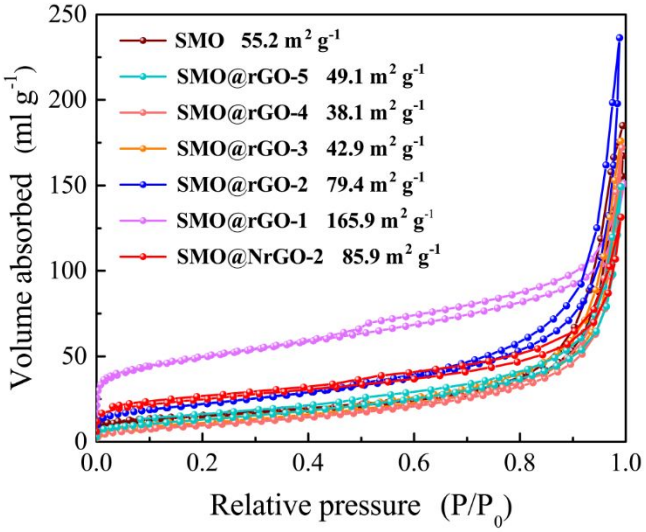

Figure S6. SSA of SMO@rGO and SMO@NrGO-2 compared with pure SMO.

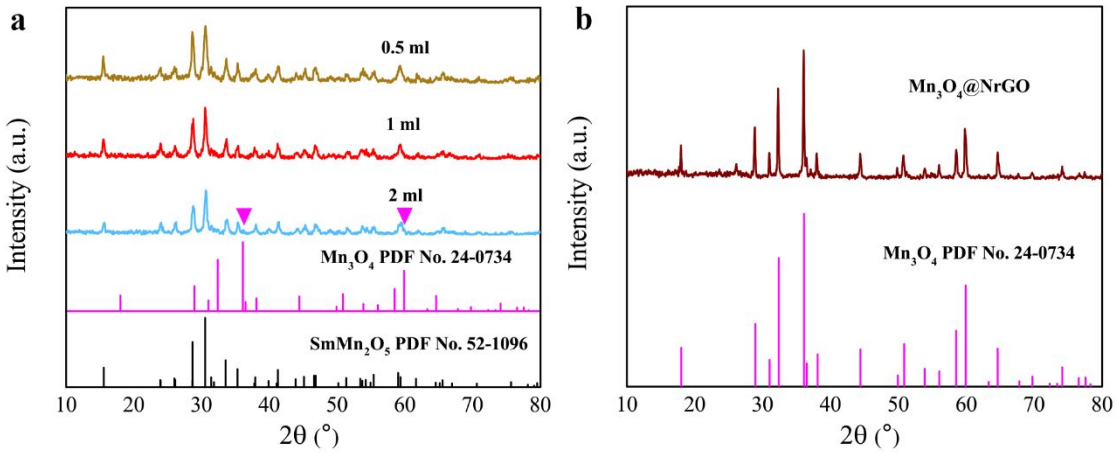

Figure S7. XRD spectra of (a) SMO@NrGO-2 prepared with different amount of ammonia and (b) the sample prepared by adding 1 ml ammonia but without Sm precursor.

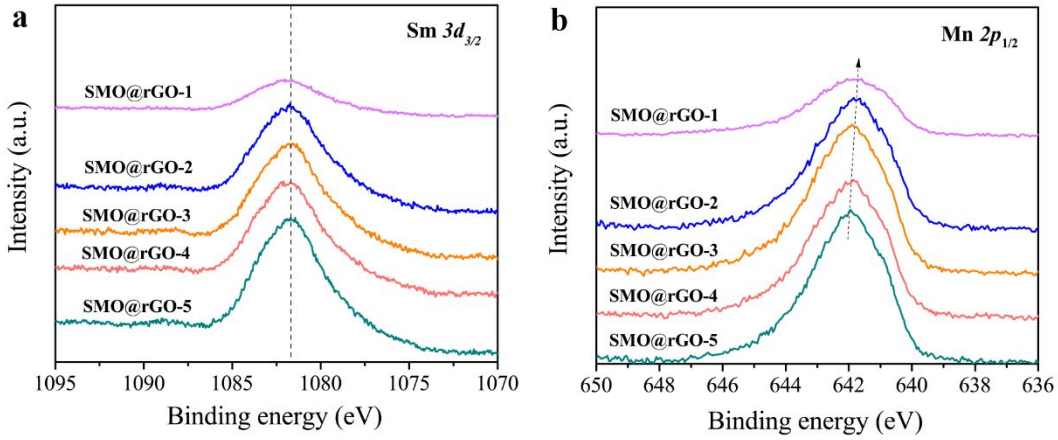

Figure S8. XPS spectra of Sm $3d_{3/2}$ and Mn $2p_{1/2}$ of SMO@rGO-x.

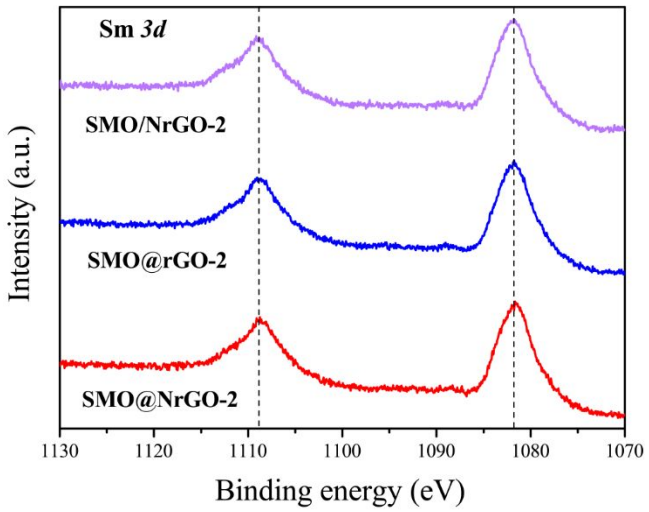

Figure S9. XPS Sm *3d* spectra of SMO/NrGO-2, SMO@rGO-2 and SMO@NrGO-2.

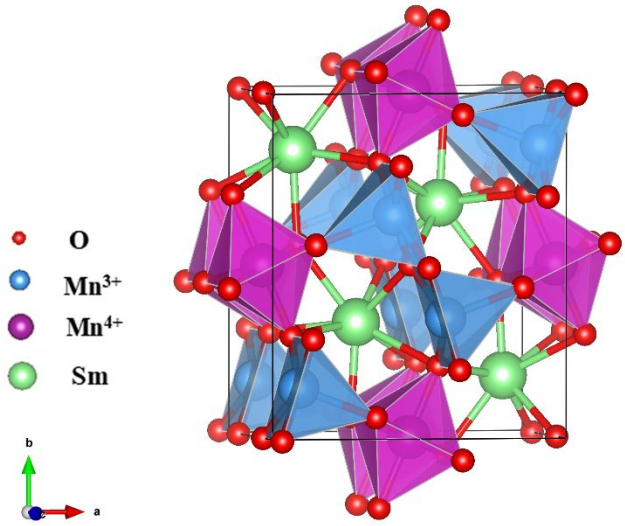

Figure S10. Crystal structure of a (1×1×1) $SmMn_2O_5$ unit cell. The square pyramid and octahedron represent crystalline field of the Mn^{3+} and Mn^{4+}. The O, Mn^{3+}, Mn^{4+} and Sm atoms are labeled as red, blue, violet and green, respectively.

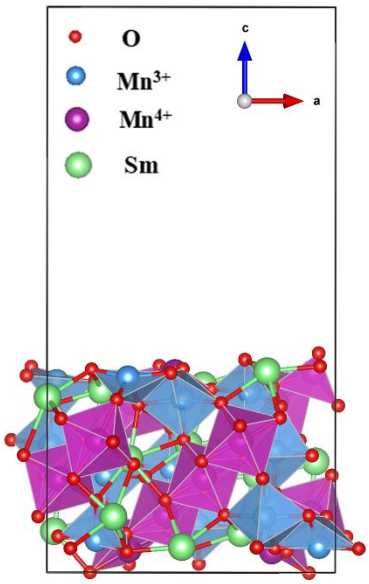

Figure S11. Side view of the $SmMn_2O_5$ (121) slab. The O, Mn^{3+}, Mn^{4+} and Sm atoms are labeled as red, blue, violet and green, respectively.

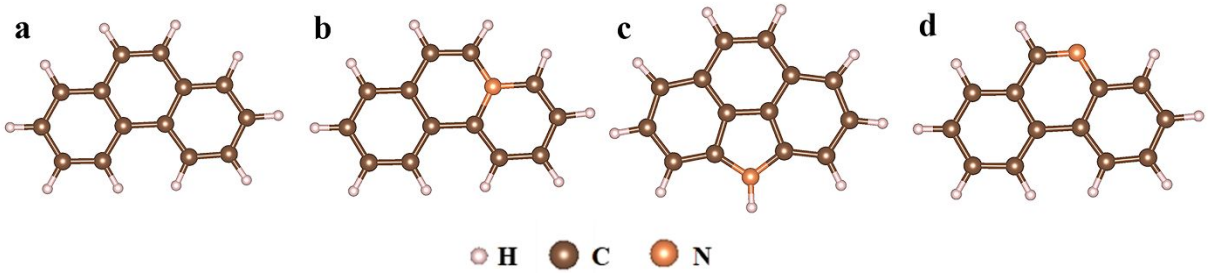

Figure S12. Structures of (a) pure graphene, (b) graphitic N (c) pyrrolic N and (d) pyridinic N. White, brown and orange balls represent H, C and N, respectively.

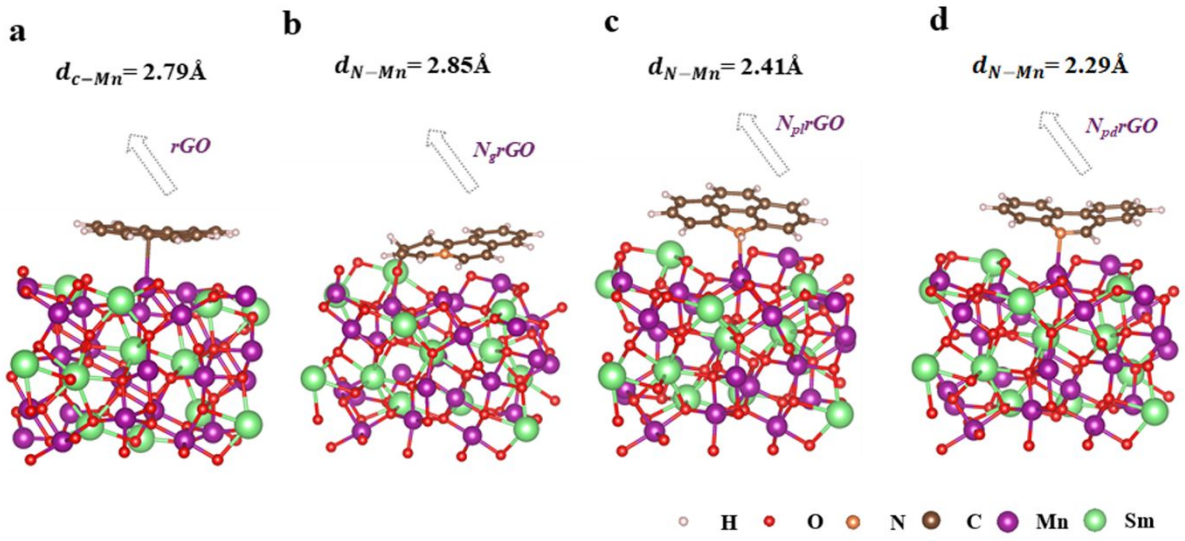

Figure S13. Bond lengths of Mn-C or Mn-N in (a) SMO@rGO (b) SMO@Gra-NrGO (c) SMO@Pyrr-NrGO and (d) SMO@Pyri-NrGO. White, red, orange, brown, violet and green balls represent H, O, N, C, Mn and Sm, respectively.

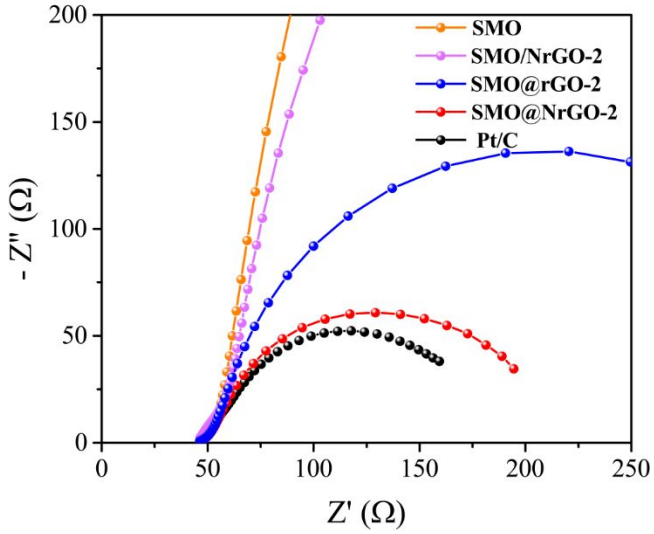

Figure S14. EIS of SMO, SMO/NrGO-2, SMO@rGO-2, SMO@NrGO-2 and Pt/C at 0.85 V.

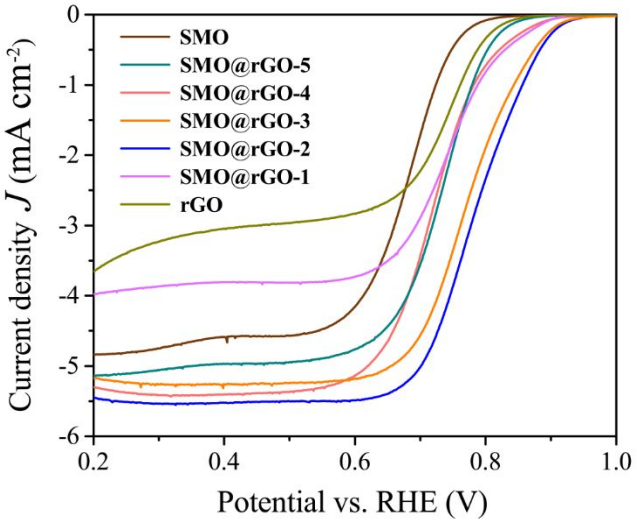

Figure S15. LSV curves of SMO@rGO-x compared with pure SMO and rGO.

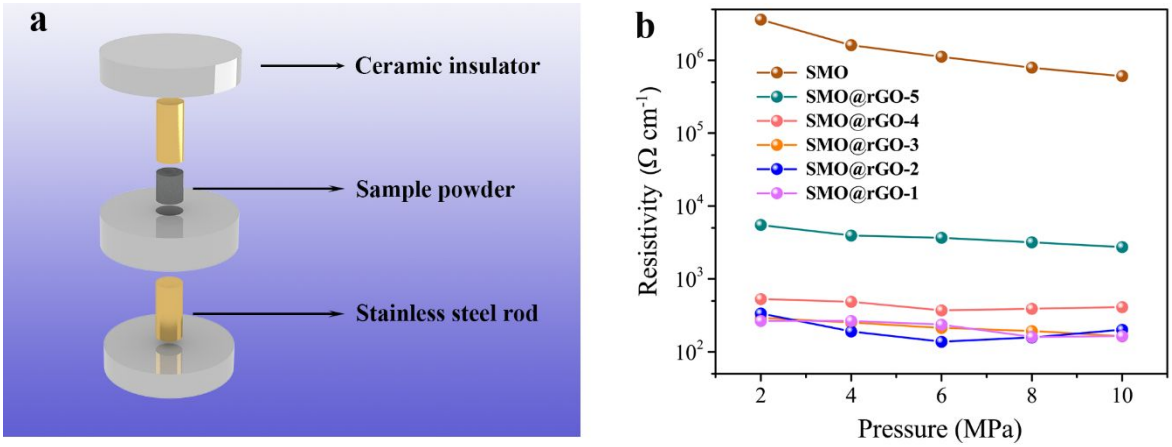

Figure S16. (a) Illustration of the home-made configuration for powder resistivity evaluation. (b) The powder resistivity of SMO@rGO-x compared with pure SMO.

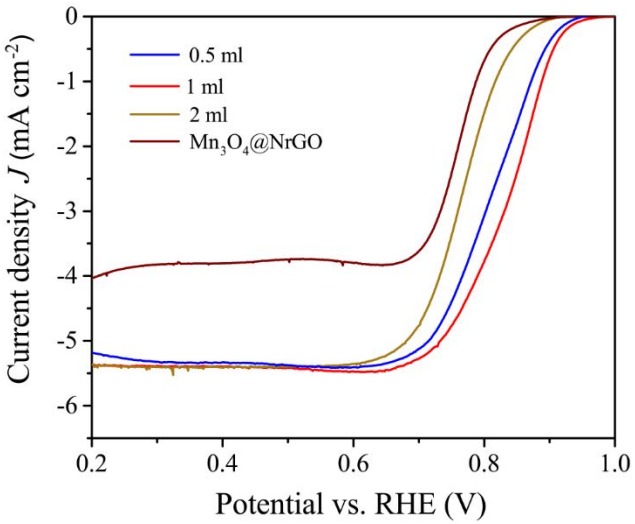

Figure S17. LSV curves of SMO@NrGO-2 prepared with different amount of ammonia compared with the sample prepared without Sm (Mn_3O_4@NrGO).

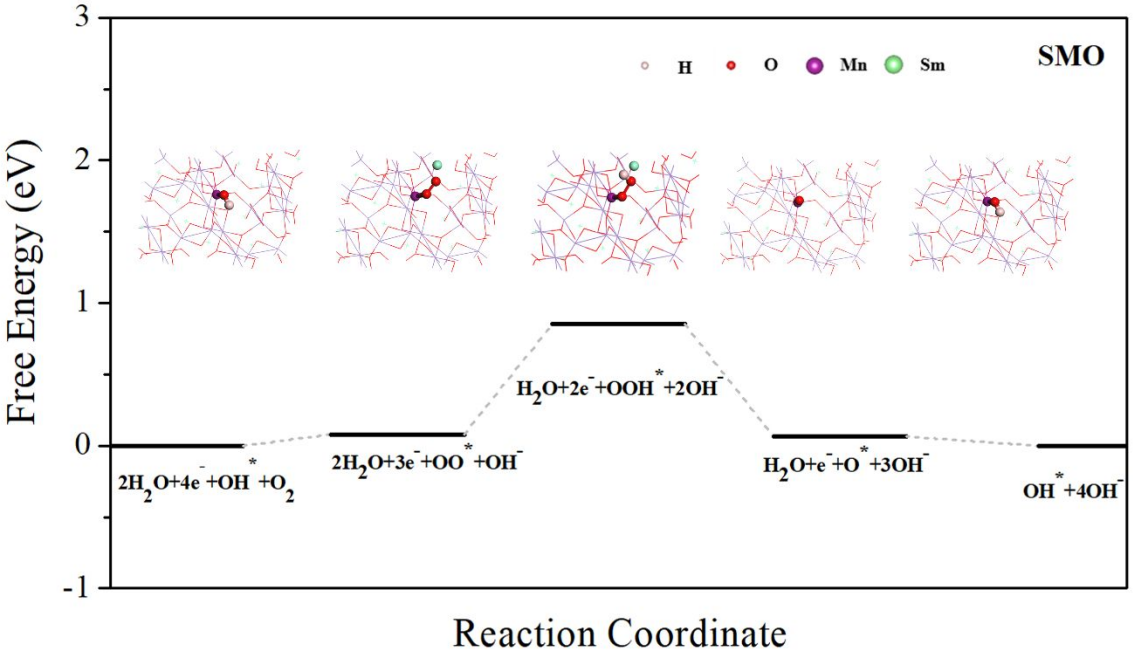

Figure S18. The free energy diagram of ORR on SMO at the equilibrium potential and the adsorption states of oxygenates are shown in the illustrations.

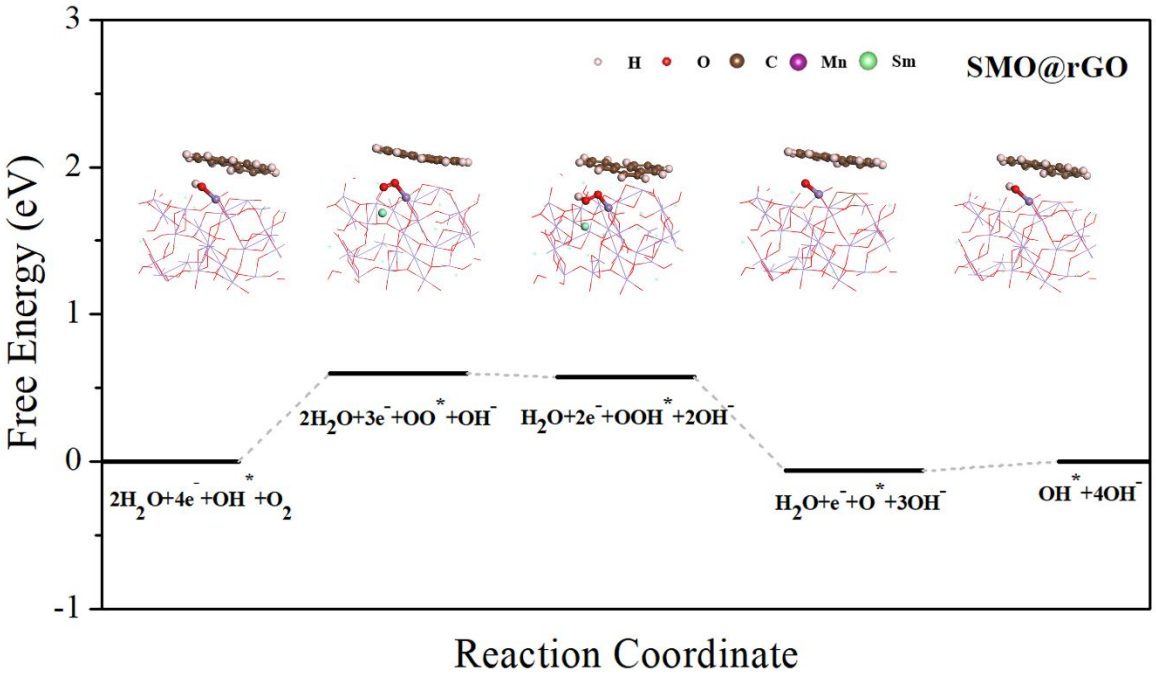

Figure S19. The free energy diagram of ORR on SMO@rGO at the equilibrium potential and the adsorption states of oxygenates are shown in the illustrations.

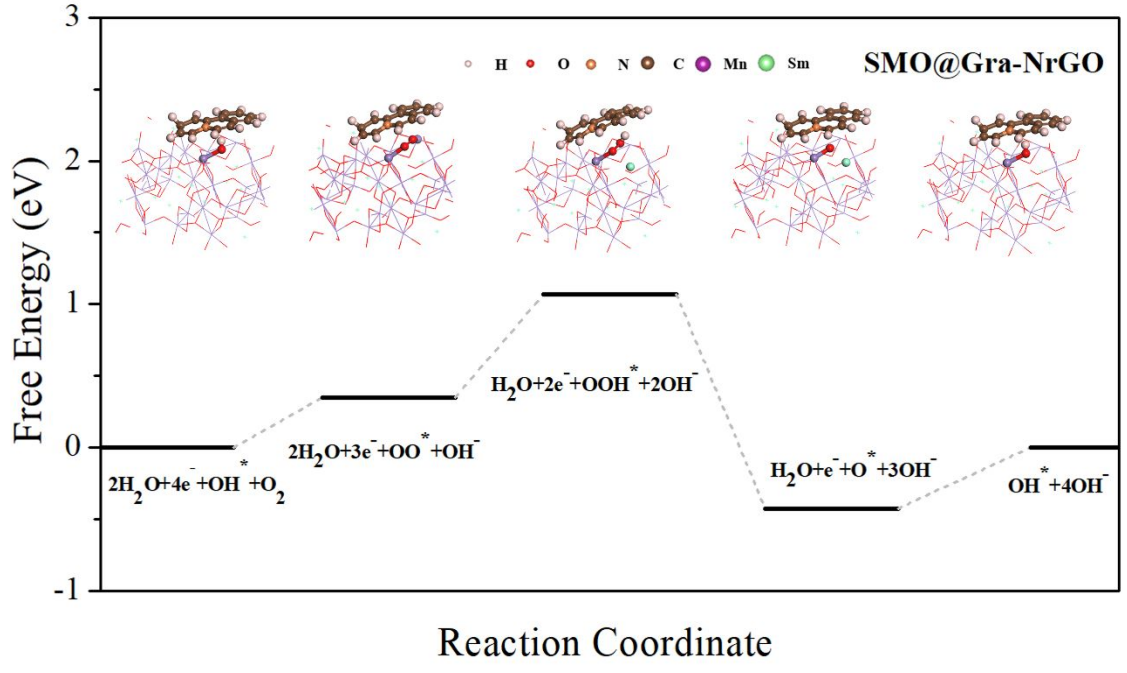

Figure S20. The free energy diagram of ORR on SMO@Gra-NrGO at the equilibrium potential and the adsorption states of oxygenates are shown in the illustrations.

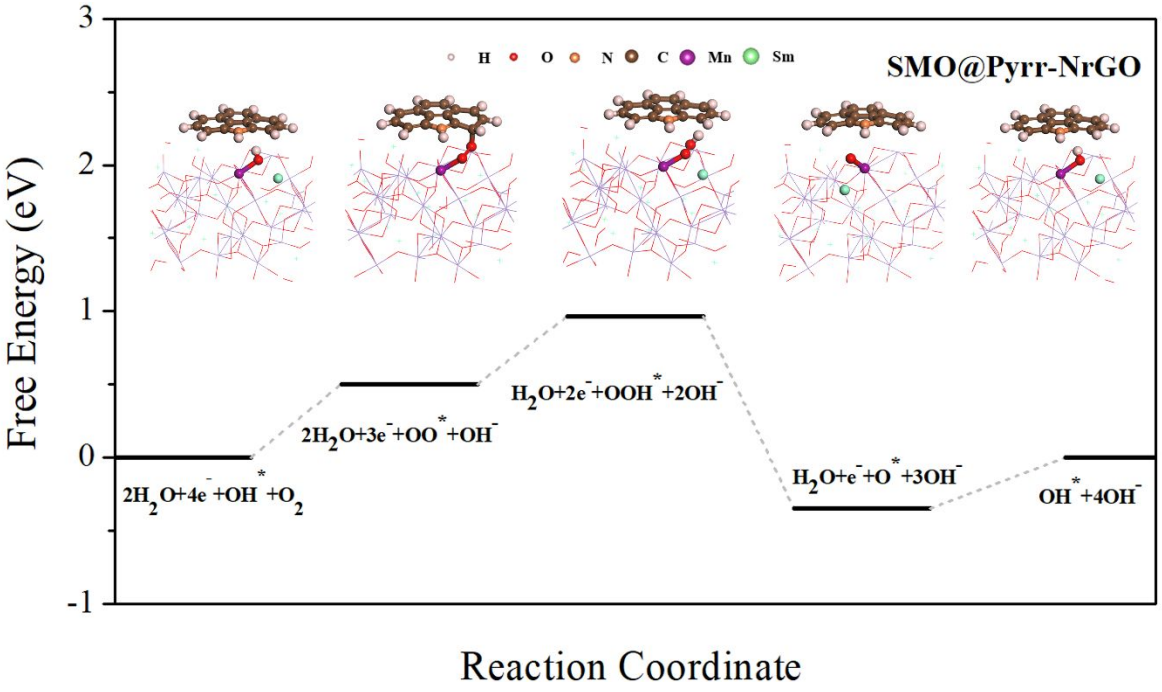

Figure S21. The free energy diagram of ORR on SMO@Pyrr-NrGO at the equilibrium potential and the adsorption states of oxygenates are shown in the illustrations.

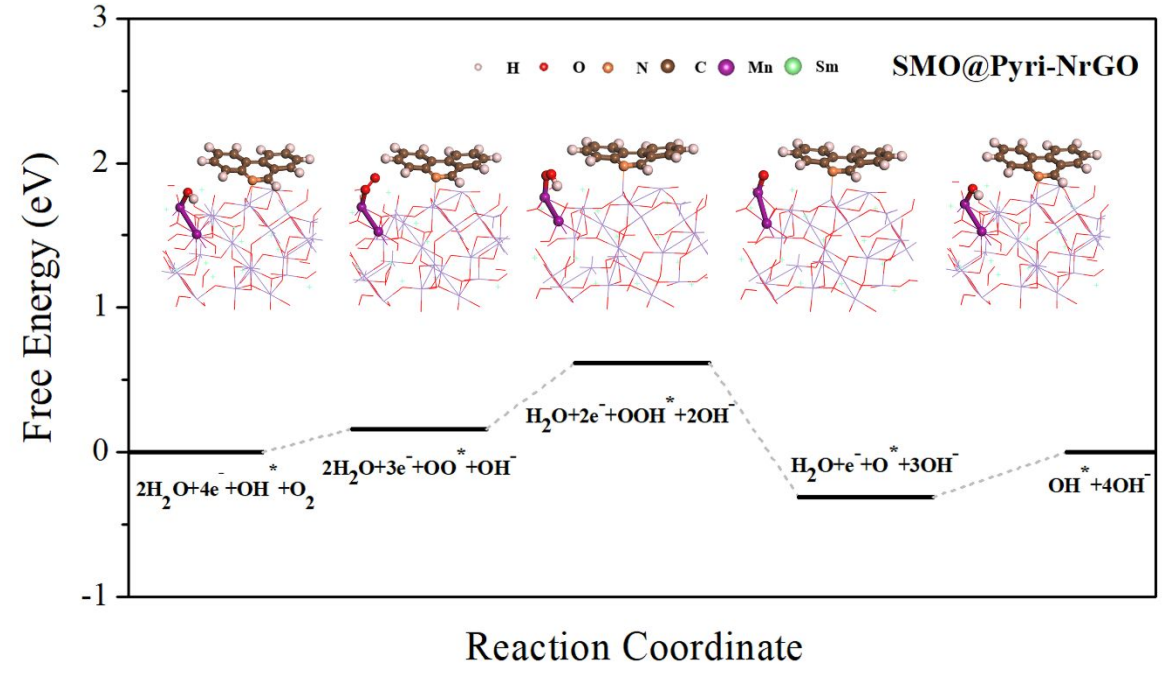

Figure S22. The free energy diagram of ORR on SMO@Pyri-NrGO at the equilibrium potential and the adsorption states of oxygenates are shown in the illustrations.

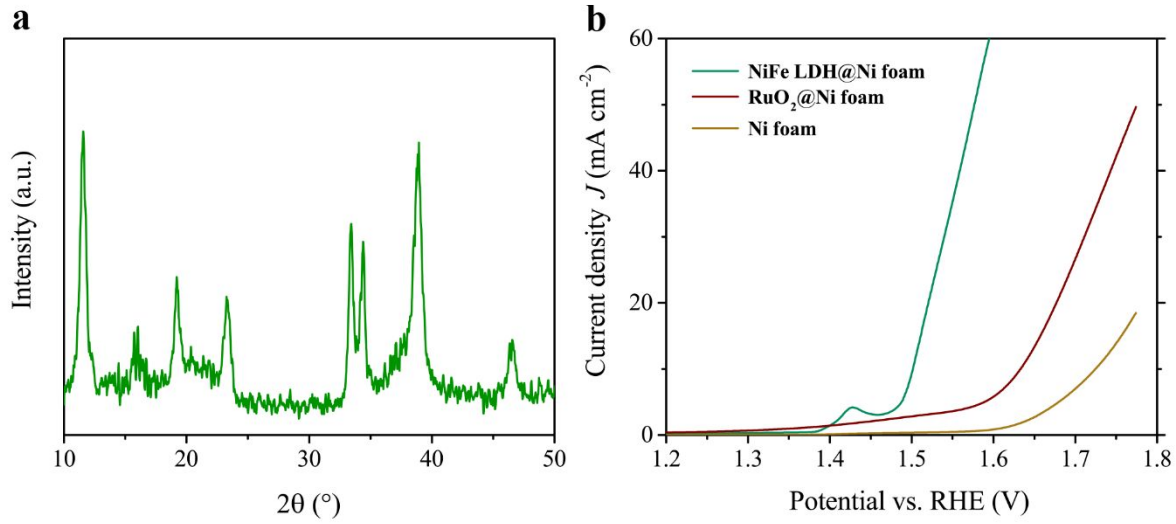

Figure S23. (a) XRD and (b) the corresponding LSV curve of NiFe LDH. LSV curved of Ni foam loaded RuO_2 nanoparticles and pure Ni foam were also provided as reference.

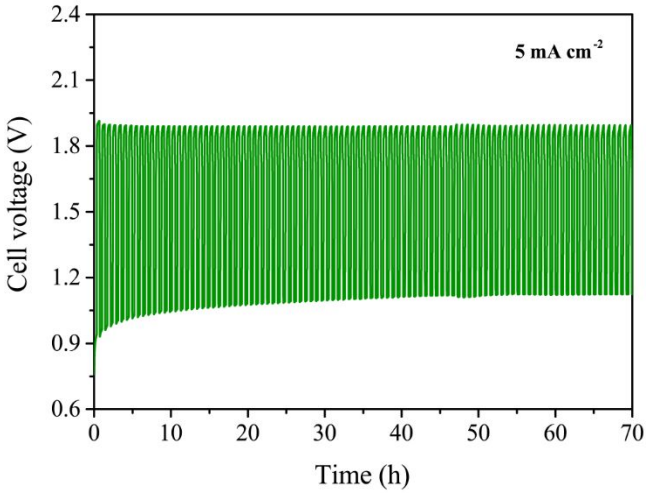

Figure S24. The cycling performance of rechargeable ZAB made with NiFe LDH only.

Table S1. Mass loading of different samples

Sample	SMO@rGO-5	SMO@rGO-4	SMO@rGO-3	SMO@rGO-2	SMO@rGO-1	SMO@NrGO-2
SMO% calculated from feeding ratio	83.3%	80%	75%	66.7%	50%	66.7%
SMO% calculated from TGA	90.4%	85.0%	80.2%	73.9%	40.9%	72.8%

Table S2. Zero point energy corrections (ZPE) and entropic correction (TS) for ORR intermediates, which absorbed on the $SmMn_2O_5$ (121) surface at 300K.

	TS	TΔS	ZPE	ΔZPE	ΔZPE − TΔS
H_2O	0.670	0	0.560	0	0
O*+H_2	0.410	-0.260	0.347	-0.213	0.047
OH*+1/2H_2	0.205	-0.465	0.492	-0.068	0.397
OO*+2H_2	0.820	-0.520	0.692	-0.428	0.092
OOH*+3/2H_2	0.615	-0.725	0.860	-0.260	0.465
H_2	0.410	0	0.270		
O*	0		0.077		
OH*	0		0.357		
OO*	0		0.152		
OOH*	0		0.455		

Table S3. Zero point energy corrections (ZPE) and entropic correction (TS) for ORR intermediates, which absorbed on the $SmMn_2O_5$@rGO at 300K.

	TS	TΔS	ZPE	ΔZPE	ΔZPE − TΔS
H_2O	0.670	0	0.560	0	0
O*+H_2	0.410	-0.260	0.349	-0.211	0.049
OH*+1/2H_2	0.205	-0.465	0.505	-0.055	0.410
OO*+2H_2	0.820	-0.520	0.694	-0.423	0.094
OOH*+3/2H_2	0.615	-0.725	0.866	-0.254	0.471
H_2	0.410	0	0.270		
O*	0		0.079		
OH*	0		0.370		
OO*	0		0.154		
OOH*	0		0.461		

Table S4. Zero point energy corrections (ZPE) and entropic correction (TS) for ORR intermediates, which absorbed on the $SmMn_2O_5$@Gra-NrGO at 300K.

	TS	TΔS	ZPE	ΔZPE	ΔZPE − TΔS
H_2O	0.670	0	0.560	0	0
O*+H_2	0.410	-0.260	0.351	-0.209	0.051
OH*+1/2H_2	0.205	-0.465	0.506	-0.054	0.411
OO*+2H_2	0.820	-0.520	0.690	-0.430	0.090
OOH*+3/2H_2	0.615	-0.725	0.863	-0.257	0.468
H_2	0.410	0	0.270		
O*	0		0.081		
OH*	0		0.371		
OO*	0		0.150		
OOH*	0		0.458		

Table S5. Zero point energy corrections (ZPE) and entropic correction (TS) for ORR intermediates, which absorbed on the $SmMn_2O_5$@Pyrr-NrGO at 300K.

	TS	TΔS	ZPE	ΔZPE	ΔZPE − TΔS
H_2O	0.670	0	0.560	0	0
O*+H_2	0.410	-0.260	0.348	-0.212	0.048
OH*+1/2H_2	0.205	-0.465	0.509	-0.051	0.414
OO*+2H_2	0.820	-0.520	0.695	-0.425	0.095
OOH*+3/2H_2	0.615	-0.725	0.864	-0.256	0.469
H_2	0.410	0	0.270		
O*	0		0.078		
OH*	0		0.374		
OO*	0		0.155		
OOH*	0		0.459		

Table S6. Zero point energy corrections (ZPE) and entropic correction (TS) for ORR intermediates, which absorbed on the $SmMn_2O_5$@Pyri-NrGO at 300K.

	TS	TΔS	ZPE	ΔZPE	ΔZPE − TΔS
H_2O	0.670	0	0.560	0	0
O*+H_2	0.410	-0.260	0.347	-0.213	0.047
OH*+1/2H_2	0.205	-0.465	0.498	-0.062	0.403
OO*+2H_2	0.820	-0.520	0.680	-0.440	0.080
OOH*+3/2H_2	0.615	-0.725	0.847	-0.273	0.452
H_2	0.410	0	0.270		
O*	0		0.077		
OH*	0		0.363		
OO*	0		0.140		
OOH*	0		0.445		

References

(1) Zhang, J.; Liu, J.; Xi, L.; Yu, Y.; Chen, N.; Sun, S.; Wang, W.; Lange, K.M.; Zhang, B. Single-Atom Au/NiFe Layered Double Hydroxide Electrocatalyst: Probing the Origin of Activity for Oxygen Evolution Reaction. *J. Am. Chem. Soc.* **2018***, 140,* 3876-3879.

(2) Hohenberg, P. and Kohn, W. Inhomogeneous Electron Gas. *Phys. Rev.* **1964**, 136, B864-B871.

(3) Kresse, G. and Hafner, J. Ab Initio Molecular-Dynamics Simulation of the Liquid-Metal-Amorphous-Semiconductor Transition in Germanium. *Phys. Rev. B* **1994**, 49, 14251-14269.

(4) Perdew, J.P.; Burke, K. and Ernzerhof, M. Generalized Gradient Approximation Made Simple. *Phys. Rev. Lett.* **1996**, 77, 3865-3868.

(5) Kresse, G. and Joubert, D., 1999. From Ultrasoft Pseudopotentials to the Projector Augmented-Wave Method. *Phys. Rev. B* **1999**, 59, 1758-1775.

(6) Grimme, S.; Antony, J.; Ehrlich, S. and Krieg, H. A. Consistent and Accurate ab Initio Parametrization of Density Functional Dispersion Correction (DFT-D) for the 94 Elements H-Pu. *J. Chem. Phys.* **2010**, DOI: 10.1063/1.3382344

(7) Wang, X.-R.; Liu, J.-Y.; Liu, Z.-W.; Wang, W.-C.; Luo, J.; Han, X.-P.; Du, X.-W.; Qiao, S.-Z.; Yang, J. Identifying the Key Role of Pyridinic-N-Co Bonding in Synergistic Electrocatalysis for Reversible ORR/OER. *Adv. Mater.* **2018**, DOI: 10.1002/adma.201800005.